Elastic strain energy and pore-fluid pressure control of aftershocks

*Toshiko Terakawa[1], Mitsuhiro Matsu'ura[2], Akemi Noda[3]

1. Graduate School of Environmental Studies, Nagoya University, D2-2 (510) Furo-cho, Chikusa-ku, Nagoya 464-8601, Japan

2. Institute of Statistical Mathematics, 10-3 Midori-cho, Tachikawa, Tokyo 190-8562, Japan

3. National Research Institute for Earth Science and Disaster Resilience, 3-1 Tennodai, Tsukuba, Ibaraki 305-0006, Japan

E-mail: terakawa@seis.nagoya-u.ac.jp

Abstract

Aftershocks are well-known, however their triggering mechanisms remain unclear. The Coulomb failure stress change (ΔCFS) has been widely implemented to understand the spatial distribution of aftershocks. Here we propose a new metric for evaluating aftershock generation based on the energetics of shear faulting in a prestressed state. Unlike ΔCFS, the new metric depends not only on coseismic stress changes but also on background crustal stresses. The energetics-based formulation expands the ΔCFS defined on a specific plane into a generalized failure stress defined in a three-dimensional space. We examined the diagnostic ability of the new metric by applying receiver operating characteristic analysis to 12,175 aftershocks ($M \geq 0$) that followed the 1992 Landers earthquake. With a realistic background stress field inferred from thousands of earthquake focal mechanisms, the new metric was able to discriminate the triggering mechanisms of the aftershocks: two-thirds were direct responses to coseismic stress changes and one-fifth resulted from strength decreases owing to pore-fluid pressure increases.

Keywords

elastic strain energy, earthquake generation, background stress, pore-fluid pressure, Landers earthquake, ROC analysis

1. Introduction

Recently, machine-leaning techniques have come to be increasingly used for forecasting aftershocks (e.g., DeVries et al., 2018; Mignan and Broccardo, 2019). A deep learning neural network model (DeVries et al., 2018) trained by the coseismic stress changes and aftershock hypocenters of more than 131,000 main shock–aftershock pairs in the worldwide database, showed its power to more accurately forecast the spatial patterns of aftershocks than does the classic Coulomb failure stress change (ΔCFS) (e.g., Reasenberg and Simpson, 1992; Stein et al., 1992; King et al., 1994; Hardebeck et al., 1998; Kilb et al., 2002; Toda et al., 2011). Based on the similarity between the spatial patterns of the predicted probability of aftershocks and those of various stress metrics, the deep learning approach suggests that the maximum change in shear stress ($\Delta\tau_{max}$), or the square root of the second invariant of a deviatoric stress change tensor, controls the occurrence of aftershocks more critically than does ΔCFS.

In general, maximum shear stress is proportional to the square root of the second invariant of a deviatoric stress tensor, which itself is proportional to the shear strain energy (Jaeger, 1962). Then, $\Delta\tau_{max}$ caused by a main shock is proportional to the square root of the coseismic change in shear strain energy if (and only if) the deviatoric stress field before the main shock is zero everywhere; that is, the preseismic shear strain energy is zero everywhere. In such a case, the coseismic change in shear strain energy is positive everywhere (Matsu'ura et al., 2019). Therefore, the metric of $\Delta\tau_{max}$ suggested by the deep learning approach seems to contradict the principle that earthquakes are shear faulting to release elastic strain energy in the Earth's crust.

The most likely cause of this unreasonable suggestion is that the training data used in the deep learning approach were coseismic stress changes only (Meade et al.,

2017; DeVries et al., 2018). In reality, absolute crustal stress plays the most essential role in the occurrence of earthquakes. Therefore, we should not neglect the effects of background crustal stress (Saito et al., 2018; Matsu'ura et al., 2019). Moreover, aftershocks can be triggered not only by increases in shear stress but also by decreases in fault strength owing to increases in pore-fluid pressure, or decreases in effective normal stress (e.g., Hubbert and Rubey, 1959; Miller et al., 2004; Sibson, 2007; Terakawa et al., 2010, 2012, 2013; Terakawa, 2014; Goebel el al., 2017; Ellsworth et al., 2019). The latter effect is usually incorporated into the ΔCFS by using Skempton's coefficients (e.g., Kilb et al., 2002). This treatment amounts to replacing the friction coefficient of rocks with an apparent value, however, such an approach may lead to a reduction in the effect of decreasing in fault strength.

Herein we propose an energetics-based stress metric that can explain the spatial pattern of aftershocks by considering the effects of changes in shear strain energy, volumetric strain energy, and pore-fluid pressure. To evaluate the change in elastic strain energy, all the six components of the background crustal stress must be known. In the source region of the 1992 Landers earthquake (Mw 7.3) in California, USA, the realistic background stress field has been estimated from thousands of earthquake focal mechanism data using a method of Bayesian statistical inference (Akaike, 1977, 1980; Yang et al., 2012; Terakawa and Hauksson, 2018). We studied aftershocks following the Landers earthquake to test the usefulness of the energetics-based stress metric in understanding the spatial pattern of aftershocks and their triggering mechanisms. In order to assess the diagnostic ability of the new metric, we applied the method of receiver operating characteristic (ROC) analysis to the dataset and demonstrated that

83 over-pressurised fluids as well as coseismic stress changes play important roles in
84 triggering aftershocks.
85
86 **2. An energetics-based stress metric for earthquake generation**
87 The Coulomb failure stress (*CFS*) is generally defined by the difference between shear
88 stress τ and fault strength τ_s for a specific receiver fault, and its change caused by a
89 seismic event, $\Delta CFS \equiv \Delta\tau - \Delta\tau_s$ with $\Delta\tau_s = \mu'\Delta\sigma_n$ (μ': apparent friction coefficient, $\Delta\sigma$
90 $_n$: normal stress change), has played a primary role for understanding aftershock
91 generation (e.g., Reasenberg and Simpson, 1992; Stein et al., 1992; King et al., 1994;
92 Hardebeck et al., 1998; Kilb et al., 2002; Toda et al., 2011). However, although the
93 occurrence of earthquakes is governed by absolute crustal stress, the ΔCFS is evaluated
94 only from coseismic stress changes. Furthermore, the values of ΔCFS depend on the
95 orientation of receiver faults (Supplemental Figure 1). To resolve these problems, first,
96 we propose an energetics-based failure stress (*EFS*) instead of *CFS*, and explain that its
97 change (ΔEFS) gives a rational stress metric for evaluating aftershock generation. Next,
98 we demonstrate how the new stress metric reflects background stress fields as well as
99 coseismic stress changes.
100
101 **2.1 Definition of ΔEFS**
102 The elastic strain energy density E is defined as half of the product of stress tensor σ_{ij}
103 and strain tensor ε_{ij}, which can be divided into shear strain energy density E_s and
104 volumetric strain energy density E_v as follows (Jaeger, 1962; Matsu'ura et al., 2019):
105 $$E \equiv \frac{1}{2}\sigma_{ij}\varepsilon_{ij} = E_s + E_v \quad (1)$$

with

$$E_s = (4G)^{-1}\sigma'_{ij}\sigma'_{ij} = (2G)^{-1}J_2(\sigma'_{ij}), \tag{2}$$

$$E_v = (18\kappa)^{-1}\sigma^2_{\alpha\alpha} = (2\kappa)^{-1}\left[\tfrac{1}{3}I_1(\sigma_{ij})\right]^2, \tag{3}$$

where G and κ are rigidity and bulk modulus, and I_1 and J_2 are the first invariant of stress tensor σ_{ij} and the second invariant of deviatoric stress tensor $\sigma'_{ij} = \sigma_{ij} - \frac{1}{3}\sigma_{\alpha\alpha}\delta_{ij}$, respectively. We defined an energetics-based failure stress (*EFS*) as

$$EFS = \sqrt{2GE_s} - \mu\left(\sqrt{2\kappa E_v} - P_f\right), \tag{4}$$

where μ and P_f are friction coefficient and pore-fluid pressure, respectively. The term $\sqrt{2GE_s}$ is the square root of the second invariant of a deviatoric stress tensor, which is a scalar metric of shear stress (Appendix A). On the other hand, the term $\sqrt{2\kappa E_v}$ is one-third of the first invariant of a stress tensor; that is the mean normal stress. Therefore, the second term on the right-hand side corresponds to the frictional strength of a fault. Positive changes in shear stress and negative changes in fault strength would promote the triggering of an earthquake and vice versa.

From Eq. (4), the change in *EFS* due to a seismic event can be written as

$$\begin{aligned}\Delta EFS = &\left[\sqrt{2G(\bar{E}_s + \Delta E_s)} - \sqrt{2G\bar{E}_s}\right] \\ &- \mu\left[\left(\sqrt{2\kappa(\bar{E}_v + \Delta E_v)} - \sqrt{2\kappa\bar{E}_v}\right) - \Delta P_f\right]\end{aligned} \tag{5}$$

with

$$\Delta E_s = (2G)^{-1}(\bar{\sigma}'_{ij} + \tfrac{1}{2}\Delta\sigma'_{ij})\Delta\sigma'_{ij} \tag{6}$$

$$\Delta E_v = (9\kappa)^{-1}(\bar{\sigma}_{\alpha\alpha} + \tfrac{1}{2}\Delta\sigma_{\alpha\alpha})\Delta\sigma_{\alpha\alpha}, \tag{7}$$

where $\bar{\sigma}_{ij}$, $\Delta\sigma_{ij}$, and ΔP_{f} are a background crustal stress tensor, a coseismic stress change tensor, and pore-fluid pressure change, respectively. We use the Δ*EFS* associated with the occurrence of a main shock as a metric for evaluating the spatial pattern of aftershocks. The decrease in fault strength generally results from a decrease in fault normal stress and/or an increase in pore-fluid pressure. Here, we use Δ*EFS** to denote Δ*EFS* without considering the effects of coseismic pore-fluid pressure changes.

The essential difference between Δ*EFS* from Δ*CFS* is that the former depends on both coseismic stress changes and background stress fields (Saito et al., 2018; Matsu'ura et al, 2019), whereas the latter focuses only on the effects of coseismic stress changes. Furthermore, both shear stress and fault strength in *EFS* are described using elastic strain energies, which enables us to evaluate the occurrence of aftershocks without specifying the orientation of a receiver fault. In other words, Δ*EFS* can expand Δ*CFS*, which is defined on a specific fault plane, into a generalized failure stress change defined in a three-dimensional stress space. When the background stress field is isotropic (e.g., the lithostatic stress state with no deviatoric stress) and the coseismic stress change is pure shear, Δ*EFS** is reduced to $\Delta\tau_{\max}$ (Appendix A).

2.2 Dependence of Δ*EFS* on background stress fields

The background stress field immediately before the 1992 Landers earthquake is characterized by a single dimensionless parameter of pore-fluid pressure ratio, *C* (strictly speaking, 1 – *C*), which provides a scaling factor of the background deviatoric stress field (Appendix B) (Terakawa and Hauksson, 2018). We calculated the values of ΔE_{s}, ΔE_{v}, and Δ*EFS** due to coseismic stress changes for four background stress fields with different deviatoric stress levels (Fig. 1). Here, we used the coseismic stress

149 changes calculated with the analytical slip response function (Fukahata and Matsu'ura,
150 2005, 2006) and a fault rupture model based on the study of Wald and Heaton (1994)
151 (Figures 4 and S3 of Terakawa and Hauksson, 2018). First and second Lame's constants
152 of 40 GPa, as well as a friction coefficient of 0.6, were used in the calculations. The first
153 three background stress fields are characterized by C = 0.0, 0.5, and 0.8, respectively.
154 The fourth is the lithostatic stress field with no deviatoric stress, which is formally
155 characterized by C = 1.0. Essentially, the change in shear strain energy ΔE_s is negative
156 (positive) in regions where the coseismic change in deviatoric stress occurs in the
157 opposite (same) direction to the background deviatoric stress. However, when the
158 background deviatoric stress level is much lower than the magnitude of the coseismic
159 stress change, the second invariant term of the deviatoric stress change tensor becomes
160 dominant (Matsu'ura et al., 2019); therefore, the change in shear strain energy becomes
161 positive everywhere (Fig. 1J).

162 On the other hand, the change in the volumetric strain energy ΔE_v depends on the
163 isotropic component of the background stress field. In the present case, where the
164 isotropic stress component is regarded as lithostatic pressure, the value of ΔE_v is not
165 controlled by parameter C (Figs 1B, E, H, and K); that is, the change in volumetric
166 strain energy is positive (negative) in regions where the stress change caused by the
167 right lateral strike−slip faulting of the Landers earthquake is compression (expansion).

168 Finally, combining the effects of ΔE_s and ΔE_v, we obtained the spatial patterns of
169 ΔEFS^* (Figs 1C, F, I, and L). The values of ΔEFS^* tend to be negative near the main
170 rupture zone, where a decrease in ΔE_s is dominant because of the large shear stress
171 release caused by the main rupture (Figs 1C, and F). In contrast, as the background

deviatoric stress level decreases, the second invariant term of the deviatoric stress change tensor becomes dominant, which is positive everywhere (Figs 1I, and L). As demonstrated in Fig. 1, changes in elastic strain energy due to the main shock strongly depend on the background deviatoric stress level characterized by C. The most realistic value of C in the source region of the Landers event has been estimated to be 0.0, which is consistent with the fundamental constraint that the amount of elastic strain energy released by the main shock must be at least larger than the amount of seismic wave energy radiated from the source (i.e., 4.3×10^{16} Nm) (Kanamori et al., 1993; Terakawa and Hauksson, 2018).

3. The diagnostic ability of Δ*EFS*

The Landers earthquake occurred on June 28, 1992 at the southern end of the eastern California shear zone. It was followed by more than ten thousand aftershocks. We focussed on the three-dimensional region surrounding the main rupture zone (lon: 115.8ºW–117.6ºW, lat: 33.6ºN–35.0ºN, depth: 2.5–12.5 km) to test the diagnostic ability of Δ*EFS* in forecasting the spatial pattern of the aftershocks, using the ROC analysis. The analysis technique is widely used to evaluate the validity of medical diagnostic tests.

First, we gridded the study region into $5\times5\times5$ km^3 cells and determined the values of ΔE_s, ΔE_v, and ΔEFS^* at the centroid of every cell for the case of $C = 0.0$ (the most realistic background stress field) without considering the effects of coseismic pore-fluid pressure changes (Figs 1A–C). Next, we estimated the three-dimensional pore-fluid pressure fields from 2136 and 1970 focal mechanism data ($M \geq 1$) for the pre-mainshock (1 January 1981 to 28 June 1992) and post-mainshock (28 June 1992 to

196 27 June 1993) periods, respectively (Figs 2A–B) (Terakawa et al., 2010, 2012). Finally,
197 considering the effects of coseismic changes in both pore-fluid pressure and stress
198 fields, we evaluated Δ*EFS*. We considered only coseismic changes in pore-fluid
199 pressures around the main rupture zone into account in this calculation (Fig. 2C) (e.g.,
200 Lucente et al., 2010; Savage, 2010; Terakawa et al., 2010).

201 In each grid cell, we counted the number of aftershocks for one year following the
202 main shock (Yang et al., 2012). For the dataset (number of data = 12,175, $M \geq 0$, depth:
203 2.5–12.5 km), the diagnostic abilities of ΔE_s, ΔE_v, Δ*EFS**, and Δ*EFS* were examined
204 using ROC curves, which are graphical plots of true positive rates (sensitivity) against
205 false positive rates (1– specificity) of a binary classifier for grid cells with and without
206 aftershocks over all the possible thresholds (Fig. 3). From Fig. 3A, we can see that the
207 ROC curves for ΔE_s and ΔE_v are generally plotted above and below, respectively, the
208 straight random guess line. This indicates that ΔE_s and ΔE_v have positive and negative,
209 respectively, correlations with aftershock triggering, which is consistent with the
210 physical meaning of these quantities. The diagnostic ability of Δ*EFS** is stronger than
211 that of ΔE_s because the effects of fault strength change resulting from the change in
212 fault normal stress are incorporated into Δ*EFS**. The area under the ROC curve (AUC)
213 for Δ*EFS** is 0.682, which is significantly larger than that for ΔE_s (0.623).

214 The diagnostic ability of Δ*EFS* increases further when we consider the effects of
215 coseismic changes in pore-fluid pressures (Fig. 3A). The AUC for Δ*EFS* when
216 including the effects of pore-fluid pressure change reached 0.759. The true positive rate
217 at the point where the Youden's index (true positive rate – false positive rate) takes its
218 maximum value increased from 0.553 to 0.629, whereas the false positive rate
219 decreased from 0.164 to 0.159. These results indicate that incorporating the effects of

220 coseismic pore-fluid pressure change into Δ*EFS* enables to more effectively evaluate the
221 spatial pattern of aftershocks.

222 We also examined the diagnostic ability of Δ*EFS** for the three background stress
223 fields with lower deviatoric stress levels (C = 0.5, 0.8, and 1.0) (Fig. 3B). The true
224 positive rates at the maximum Youden's index points increased from 0.553 to 0.686 as
225 the background deviatoric stress level decreased (Table 1). However, the false positive
226 rates at the same points also increased from 0.164 to 0.342. This indicates that the stress
227 metric Δ*EFS** tends to overestimate the potential regions of aftershocks when the
228 assumed background deviatoric stress level is much lower than the actual level (Figs 1F,
229 I, and L). This overestimation is marked especially in the vicinity of the main rupture
230 zone, because large coseismic stress changes contribute more significantly to increases
231 in ΔE_s. This apparent improvement in the diagnostic ability of Δ*EFS** suggests that a
232 substantial proportion of aftershocks near the main rupture zone may have occurred in
233 response to factors other than coseismic stress changes, though it is technically difficult
234 to estimate coseismic stress changes there in high resolution. In this regard, our results
235 suggest that the coseismic change in pore-fluid pressure is a plausible explanation (Figs
236 2C and Fig. 3A).
237
238 **4. Physical mechanisms for aftershock generation**

239 In the case of a realistic background stress field (C = 0.0), we examined the triggering
240 mechanisms of aftershocks (Fig. 4). For this purpose, we first counted the numbers of
241 events in each grid cell for one year before and after the Landers event (Yang et al.,
242 2012), and then evaluated the seismicity rate change for each grid cell (Supplemental
243 Figure 2). Of the total 12,175 events in the original dataset, 11,375 events (93.4 %)

occurred in the regions (grid cells) where the seismicity rate increased following the main shock. Of the 11,375 aftershocks, 7,728 events (67.9 %) occurred in regions with positive ΔEFS^*, indicating that these events were essentially triggered by coseismic stress changes. In more detail, 3,800 events (33.4 %) were triggered by the combined effect of an increase in shear stress and a decrease in fault strength. The Big Bear earthquake (M_w 6.5), which was the largest aftershock following the Landers event, is consistent with triggering produced by the combined effect. On the other hand, 3,288 events (28.9 %) were triggered by an increase in shear stress, whereas 635 events (5.6 %) were triggered by a decrease in fault strength.

Of the remaining 3,652 aftershocks, which are not consistent with ΔEFS^*, 2,435 events (21.4 %) occurred in regions with positive ΔEFS, indicating that decreasing fault strength due to increasing in pore-fluid pressure would have played a role in their triggering. We cannot explain the triggering mechanism of the remaining 1,217 events (10.7 %), even when the effects of pore-fluid pressure changes are considered. The mechanism may be related to small-scale heterogeneity in the background stress field, coseismic stress changes, and pore-fluid pressure changes, dynamic triggering, and/or secondary static stress changes caused by aftershocks (e.g., Meier et al., 2014; Kilb et al., 2002). In addition, it may be attributed to difficulty in handling on-fault aftershocks, as pointed out in the section 3.

Of the total 12,175 events in the original dataset, 775 events (6.4 %) occurred in the regions where the seismicity rate decreased following the main shock. The remaining 25 events (0.2 %) occurred in the regions where the seismicity rate did not change. The occurrence of these events may be controlled by tectonic loading in southern California.

5. Discussion

The diagnostic abilities of many stress metrics have been previously investigated without considering the effects of background stress fields and coseismic pore-fluid pressure changes (Meade et al., 2017). From these investigations, the recent deep learning approach suggests that the maximum change in shear stress $\Delta\tau_{max}$ (and its square) may more critically control aftershock generation than does ΔCFS on the plane with similar orientation to the main shock fault (DeVries et al., 2018). Our results showed that the AUC value for $\Delta\tau_{max}$ (0.686) was slightly greater than that for ΔCFS (0.667), whereas it was remarkably smaller than that for ΔEFS (C = 0.0) under a realistic background stress field (0.759) (Fig. 3C, Table 1). It should be noted that $\Delta\tau_{max}$ is proportional to the square root of ΔE_s in the case of an isotropic background stress field without any deviatoric stress (C = 1.0), as demonstrated by the accordance of the ROC curves for these two quantities (Fig. 3D). From a physical viewpoint, $\Delta\tau_{max}$ is inappropriate as a metric for explaining the spatial pattern of aftershocks because of (i) the implicit unrealistic assumption of the background deviatoric stress level and (ii) ignorance of the effects of fault strength changes. The coseismic change in shear strain energy ΔE_s under an isotropic background stress state is positive everywhere, with peaks near the main rupture zone (Fig. 1J); therefore, $\Delta\tau_{max}$ forecasts that the occurrence of aftershocks is promoted everywhere, especially near the main rupture. Actually, because of this overestimation, the false positive rate for $\Delta\tau_{max}$ (0.406) was markedly larger than those of ΔCFS (0.089) and ΔEFS (0.159) (Fig. 3C). The values of maximum Youden's indexes for $\Delta\tau_{max}$, ΔCFS and ΔEFS (C = 0.0), which are another measures for the diagnostic abilities of metrics, were 0.302, 0.397, and 0.470, respectively (Table. 1).

292 This also indicates that the new metric Δ*EFS* proposed in this study can evaluate the
293 spatial pattern of aftershocks most correctly.

294 The sum of the absolute values of the six independent components of the
295 coseismic stress change tensor (*ABCS*) has also been suggested as a stress metric that
296 explains the spatial pattern of aftershocks more effectively than Δ*CFS* (DeVries et al.,
297 2018). This quantity depends on the choice of coordinate system. In general, the
298 occurrence of earthquakes must be controlled by certain invariants because rock failure
299 does not depend on the coordinate system. From such a physical viewpoint, *ABCS* does
300 not appear to be a good metric. To understand the physical meaning of *ABCS*, we
301 compared its ROC curve with that of the square norm of the coseismic stress change
302 tensor (*SNCS*), which is a coordinate-independent metric (Fig. 3D), and found that the
303 curves almost overlapped. Coseismic changes in shear strain energy and volumetric
304 strain energy are incorporated into *SNCS* as positive factors for triggering aftershocks
305 (Appendix A) because both the deviatoric and isotropic components of background
306 stress are implicitly assumed to be zero. Since the coseismic change in volumetric strain
307 energy is positive everywhere under the zero-background isotropic stress field, *SNCS*
308 overestimates effects of the coseismic change in volumetric strain energy as well as
309 those of shear strain energy to aftershock generation. Because of the double mistakes
310 attributed from the unrealistic assumptions on deviatoric and isotropic stress fields,
311 *SNCS* is more inappropriate as a stress metric for explaining the spatial pattern of
312 aftershocks than $\Delta\tau_{\max}$, which was demonstrated in Fig. 3D. The false positive rate at
313 the maximum Youden's index point for *SNCS* (0.441) was larger than that for $\Delta\tau_{\max}$
314 (0.406), though these values are much larger than that for Δ*EFS* in every case. The

315 value of maximum Youden's index for *SNCS* (0.264) is the smallest (worst) of all
316 metrics (Table. 1), as theoretically expected.

317 We tried to reevaluate ΔE_s, ΔE_v, ΔEFS^*, and ΔEFS after taking coseismic stress
318 changes due to the Big Bear earthquake, which occurred about three hours after the
319 main shock, as well as the Landers earthquake, under the realistic background stress
320 field with $C = 0.0$ (Supplemental Figure 3). In this calculation, we modelled the source
321 of the Big Bear event by a vertical fault with the strike of N50º, length of 18 km, width
322 of 12 km, and top depth of 4 km (e.g., King et al., 1994). We assumed a uniform left-
323 lateral strike slip of 1 m tapered to the fault edges. Since the Big Bear event released
324 shear strain energy near the source region, the total values of ΔE_s, ΔEFS^* and ΔEFS
325 became smaller than those without the effects of the Big Bear event. Then, these three
326 diagnostic abilities slightly decreased (Supplemental Figure 4). For further discussion,
327 we need to take a more realistic source model and the effects of pore-fluid pressure
328 changes into consideration.

329 Aftershocks beyond the southern edge of the main rupture zone of the Landers
330 event may have been influenced by the 23 April 1992 Joshua Tree earthquake (M_w 6.1).
331 The seismicity in the Joshua Tree region (longitude: 116.5 ºW –116.3 ºW, latitude: 33.9
332 ºN –34.1 ºN) during the period from 1 April 1992 to 27 June 1993 indicates that the
333 cumulative number of events had almost reached a ceiling by the occurrence of the
334 Landers event (Supplemental Figure 5). After the Landers event, the cumulative number
335 of events remarkably increased in the regions with $\Delta EFS^* > 0$, but slightly increased in
336 regions with $\Delta EFS^* < 0$. In fact, the seismicity rate decreased after the Landers event in
337 the east side of the Joshua Tree region, where ΔEFS^* is negative, while it increased in

338 the west side, where ΔEFS^* is positive (Figure 4). This indicates that events in the
339 Joshua Tree region were controlled by not the Joshua Tree event but the Landers event.

340 Friction coefficients of intraplate/interplate faults are still the subject matter at
341 issue. We place importance on the facts that intrinsic friction coefficients μ of rocks
342 obtained in laboratory experiments and in situ stress measurements are mostly constant
343 within the range of 0.6–0.8 under fault-normal stresses ≥200 MPa (e.g., Byerlee, 1978;
344 Zoback and Townend, 2001). With this premise, we can understand apparent friction
345 coefficients lower than the standard value to be due to high pore fluid pressure.
346 Nevertheless, if we used a much lower value of μ than 0.6 in the evaluation of ΔEFS,
347 we would underestimate the effects of ΔE_v, and the ROC curves with the lower friction
348 coefficients would be drawn between those for ΔEFS with $\mu = 0.6$ and ΔEs in Figure 3a.
349 So, the assumption of $\mu = 0.6$ would not seriously affect our conclusion.

350 In this study, we used the number of aftershocks in each region to evaluate the
351 diagnostic ability of ΔEFS with the method of ROC analysis. For this purpose, we can
352 use the seismicity rate change, when the spatial distribution of aftershocks is dense
353 enough to adequately represent the seismicity rate change as in the case of the Landers
354 earthquake (Supplemental Figure 2). Through the classification of aftershocks based on
355 ΔEFS and the seismicity rate change in the section 4, we confirmed that our findings
356 obtained through the ROC analysis will not be so modified if we use the seismicity rate
357 change instead of the number of aftershocks.

358

359 **6. Conclusions**

We proposed an energetics-based failure stress (*EFS*) instead of the Coulomb failure stress (*CFS*), and explained that its change (Δ*EFS*) gives a rational stress metric for evaluating aftershock generation. Unlike the classic Δ*CFS*, the Δ*EFS* reflects the background crustal stress as well as the coseismic stress change. With a realistic background crustal stress field, we demonstrated that Δ*EFS* robustly evaluated the spatial pattern of aftershocks that followed the Landers earthquake. Our analysis shows that along with coseismic stress changes, drastic changes in pore-fluid pressure are important in the triggering of aftershocks.

A series of ROC analyses with the Δ*EFS* showed that the potential regions of aftershock generation tend to be overestimated if the assumed background deviatoric stress level is much lower than the actual level. This means that the unrealistic assumption of the background deviatoric stress level concealed the fact that over-pressurised fluids triggered 21 % of the aftershocks in the dataset. Knowledge of the absolute level of the background crustal stress field is essentially important for understanding earthquake generation.

Appendices

A. Metrics based on elastic strain energy

The first term of *EFS* in Eq. (4) of the main text, $\sqrt{2GE_s}$, is equal to $\sqrt{3/2}$ times the shear stress acting on the octahedral planes (Jaeger, 1962). It is also equal to $\sqrt{4\left(R^2-R+1\right)/3}$ times the maximum shear stress $\tau_{\max}$, where $R=\left(\sigma_1-\sigma_2\right)/\left(\sigma_1-\sigma_3\right)$ is the ratio of the maximum, intermediate, and minimum compressive principal stresses ($\sigma_1 \geq \sigma_2 \geq \sigma_3$). When the stress field is in the state of pure shear (R = 0.5), the first and

second terms of *EFS* in Eq. (4) are equal to the shear stress and frictional strength of the maximum shear stress plane.

In a general case ($R \neq 0.5$), we can rewrite *EFS* in Eq. (4) using the shear stress $\tau_{\max}$ and normal stress σ_{n} on the maximum shear stress plane, as follows:

$$EFS = \sqrt{4\left(R^2 - R + 1\right)/3}\ \tau_{\max} - \mu\left(\sigma_{\mathrm{n}} - P_{\mathrm{f}}\right) \tag{A.1}$$

with

$$\sigma_{\mathrm{n}} = \sigma + \tfrac{1}{3}\left(2R - 1\right)\tau_{\max}, \tag{A.2}$$

where $\sigma = \frac{1}{3} I_1$ is the mean normal stress.

When the background stress field is isotropic, ΔEFS^* (ΔEFS without the effects of pore-fluid pressure changes) is represented with stress invariants of the coseismic stress change tensor, as follows:

$$\Delta EFS^* = \sqrt{\Delta J_2}\ \tau_{\max} - \mu\left(\tfrac{1}{3}\Delta I_1\right), \tag{A.3}$$

where ΔI_1 and ΔJ_2 are the first invariant of a stress change tensor and the second invariant of a deviatoric stress change tensor, respectively. When the coseismic stress change tensor is in the state of pure shear ($R = 0.5$), ΔEFS^* is reduced to the maximum change in shear stress.

The *SNCS* is a scalar metric defined by

$$SNCS = \sum_{i=1}^{3}\sum_{j=1}^{3}\Delta\sigma_{ij}^2 = \left\|\Delta\sigma'_{ij}\right\|_2^2 + \left\|\tfrac{1}{3}\Delta\sigma_{\alpha\alpha}\delta_{ij}\right\|_2^2 = 2\Delta J_2 + \tfrac{1}{3}(\Delta I_1)^2\ , \tag{A.4}$$

where $\|\ \|_2$ denotes the Frobenius norm of a second order tensor. When both the deviatoric and isotropic components of background stress are zero, the first term $2\Delta J_2$ and the second term $\frac{1}{3}(\Delta I_1)^2$ of Eq. (A.4) are equivalent to $4G\Delta E_{\mathrm{s}}$ and $6\kappa\Delta E_{\mathrm{v}}$, respectively. From Eq. (A.4), we can see that the effects of both changes in deviatoric

405 stress and isotropic stress are incorporated into the *SNCS* as positive factors for
406 triggering aftershocks independently of the background stress fields.
407
408 **B. Estimating the absolute stress field**
409 Through analysis techniques of stress inversion (Terakawa and Matsu'ura, 2008),
410 earthquake focal mechanism solutions are inverted to determine the stress pattern, or the
411 deviatoric stress tensor normalized by the maximum shear stress. For the isotropic
412 component of a stress tensor, we can rationally assume that the vertical stress at a given
413 depth is equivalent to the weight of the overburden. For the last degree of freedom, we
414 determine the maximum shear stress based on the fact that shear stress is equal to the
415 frictional strength of the fault at the time of an earthquake (Terakawa and Hauksson,
416 2018). Assuming an intrinsic standard friction coefficient of 0.6, we characterize the
417 Coulomb failure criterion by the reference pore-fluid pressure P_r at the optimally
418 oriented faults of the stress pattern. The dimensionless parameter C for the reference
419 pore-fluid pressure is used as the single parameter:
420 $$C = \left(P_r - P_h\right) / \left(P_l - P_h\right), \quad \text{(B.1)}$$
421 where P_h and P_l are hydrostatic and lithostatic pressures. As the value of C becomes
422 greater, the maximum shear stress becomes smaller. For a dataset of focal mechanism
423 solutions, we calculate the absolute stress tensors at their hypocenters immediately
424 before the main shock assuming the value of C. Applying each dataset of the absolute
425 stress tensors to an inversion scheme based on Bayesian statistical inference and
426 Akaike's Bayesian information criterion (Akaike, 1977, 1980), we can obtain an
427 absolute stress field parameterized with C.

In the source region of the 1992 Landers earthquake three absolute stress fields immediately before and after the main shock were modelled with three reference pore-fluid pressure ratios (C) of 0.0, 0.5, and 0.8 (Wald and Heaton, 1994; Fukahata and Matsu'ura, 2005, 2006; Yang et al., 2012; Terakawa and Hauksson, 2018). We directly examined the dependence of temporal changes in the elastic strain energy as well as the coseismic stress rotation on parameter C. Comparing them with observed temporal changes in physical quantities (Kanamori et al., 1993), we determined the absolute stress field and found the most plausible reference pore pressure to be hydrostatic (C = 0.0).

Data availability

The data that support the findings of this study are available at https://service.scedc.caltech.edu/eq-catalogs/FMsearch.php.

Acknowledgements We are very grateful to Dr. Debi Kilb and the anonymous reviewer for their thoughtful suggestions. We would like to thank the Editor Miaki Ishii. I would like to thank Egill Hauksson and the Southern California Earthquake Data Center for providing focal mechanism solutions in the Southern California Seismic Network catalogue. This work was supported by a Grant-in Aid for Scientific Research C (18K03801) and the Observation and Research Program for Prediction of Earthquakes and Volcanic Eruptions (MEXT).

Author contributions TT proposed the original idea of the *EFS*, conceived the study,

analyzed seismic data, and prepared for an initial draft of the manuscript. MM helped to revise the *EFS* and pointed out the importance of the relations between the *EFS* and classic stress metrics. TT, MM and AN discussed detail of this research and finalized the draft.

References

Akaike, H., 1977. On entropy maximization principle, in: Krishnaiah, P.R. (Ed.), *Application of Statistics*. North-Holland, Amsterdam, pp. 27-41.

Akaike, H., 1980. Likelihood and Bayes procedure, in: Bernardo, J.M., DeGroot, M.H., Lindley, D.V., Smith, A.F.M. (Eds.), *Bayesian Statistics*. University Press, Valencia, pp. 143-166.

Byerlee, J., 1978. Friction of rocks. Pure and Applied Geophysics 116, 615-626.

DeVries, P.M.R., Viegas, F., Wattenberg, M., Meade, B.J., 2018. Deep learning of aftershock patterns following large earthquakes. Nature 560, 632-634.

Ellsworth, W. L., D. Giardini, J. Townend, S. M. Ge, and T. Shimamoto (2019), Triggering of the Pohang, Korea, earthquake (Mw 5.5) by enhanced geothermal system stimulation, Seismological Research Letters 90(5), 1844-1858.

Fukahata, Y., Matsu'ura, M., 2005. General expressions for internal deformation fields due to a dislocation source in a multilayered elastic half-space. Geophysical Journal International 161, 507-521.

475

476 Fukahata, Y., Matsu'ura, M., 2006. Quasi-static internal deformation due to a
477 dislocation source in a multilayered elastic/viscoelastic half-space and an equivalence
478 theorem. Geophysical Journal International 166, 418-434.
479

480 Goebel, T.H.W., Weingarten, M., Chen, X., Haffener, J., Brodsky, E.E., 2017. The 2016
481 Mw5.1 Fairview, Oklahoma earthquakes: Evidence for long-range poroelastic triggering
482 at > 40 km from fluid disposal wells. Earth and Planetary Science Letters 472, 50-61.
483

484 Hardebeck, J.L., Nazareth, J.J., Hauksson, E., 1998. The static stress change triggering
485 model: Constraints from two southern California aftershock sequences. Journal of
486 Geophysical Research-Solid Earth 103, 24427-24437.
487

488 Hubbert, M.K., Rubey, W.W., 1959. Role of fluid pressure in mechanics of overthrust
489 faulting. 1. Mechanics of fluid-filled porous solids and its application to overthrust
490 faulting. Geological Society of America Bulletin 70, 115-166.
491

492 Jaeger, J.C., 1962. Elasticity, Fracture and Flow with Engineering and Geological
493 Applications. Chapman and Hall, London.
494

495 Jennings, C.W. 1994. Fault activity map of California and adjacent areas, with locations
496 and ages of recent volcanic eruptions, *Calif. Div. Mines and Geology*, Geologic Data
497 Map No. 6, map scale 1:750,000.
498

Kanamori, H., Mori, J., Hauksson, E., Heaton, T.H., Hutton, L.K., Jones, L.M., 1993. Determination of earthquake energy-release and m(l) using terrascope. Bulletin of the Seismological Society of America 83, 330-346.

Kilb, D., Gomberg, J., Bodin, P., 2002. Aftershock triggering by complete Coulomb stress changes. Journal of Geophysical Research-Solid Earth 107.

King, G.C.P., Stein, R.S., Lin, J., 1994. Static stress changes and the triggering of earthquakeS. Bulletin of the Seismological Society of America 84, 935-953.

Lucente, F.P., De Gori, P., Margheriti, L., Piccinini, D., Di Bona, M., Chiarabba, C., Agostinetti, N.P., 2010. Temporal variation of seismic velocity and anisotropy before the 2009 M-W 6.3 L'Aquila earthquake, Italy. Geology 38, 1015-1018.

Matsu'ura, M., Noda, A., Terakawa, T., 2019. Physical interpretation of moment tensor and the energetics of shear faulting. Tectonophysics 771, doi:10.1016/j.tecto.2019.228228.

Meade, B.J., DeVries, P.M.R., Faller, J., Viegas, F., Wattenberg, M., 2017. What Is Better Than Coulomb Failure Stress? A Ranking of Scalar Static Stress Triggering Mechanisms from 10(5) Mainshock-Aftershock Pairs. Geophysical Research Letters 44, 11409-11416.

522 Meier, M.A., Werner, M.J., Woessner, J., Wiemer, S., 2014. A search for evidence of
523 secondary static stress triggering during the 1992 M(w)7.3 Landers, California,
524 earthquake sequence. Journal of Geophysical Research-Solid Earth 119, 3354-3370.
525
526 Mignan, A., Broccardo, M., 2019. One neuron versus deep learning in aftershock
527 prediction. Nature 574, E1-E3. doi:10.1038/s41586-019-1582-8
528
529 Miller, S.A., Collettini, C., Chiaraluce, L., Cocco, M., Barchi, M., Kaus, B.J.P., 2004.
530 Aftershocks driven by a high-pressure CO2 source at depth. Nature 427, 724-727.
531
532 Reasenberg, P.A., Simpson, R.W., 1992. Response of regional seismicity to the static
533 stress change produced by the Loma-Prieta earthquake. Science 255, 1687-1690.
534
535 Saito, T., Noda, A., Yoshida, K., Tanaka, S., 2018. Shear Strain Energy Change Caused
536 by the Interplate Coupling Along the Nankai Trough: An Integration Analysis Using
537 Stress Tensor Inversion and Slip-Deficit Inversion. Journal of Geophysical Research-
538 Solid Earth 123, 5975-5986.
539
540 Savage, M., 2010. The role of fluids in earthquake generation in the 2009 M_W 6.3
541 L'Aquila, Italy, earthquake, and its foreshocks, Geology 38, 1055-1056.
542
543 Sibson, R.H., 2007. An episode of fault-valve behaviour during compressional
544 inversion? The 2004 M(J)6.8 Mid-Niigata Prefecture, Japan, earthquake sequence.
545 Earth and Planetary Science Letters 257, 188-199.

546

547 Stein, R.S., King, G.C.P., Lin, J., 1992. Change in failure stress on the southern San
548 Andreas fault system caused by the 1992 magnitude = 7.4 Landers earthquake, Science
549 258, 1328-1332.

550

551 Terakawa, T., 2014. Evolution of pore fluid pressures in a stimulated geothermal
552 reservoir inferred from earthquake focal mechanisms. Geophysical Research Letters 41,
553 7468-7476.

554

555 Terakawa, T., Hashimoto, C., Matsu'ura, M., 2013. Changes in seismic activity
556 following the 2011 Tohoku-oki earthquake: Effects of pore fluid pressure. Earth and
557 Planetary Science Letters 365, 17-24.

558

559 Terakawa, T., Hauksson, E., 2018. Absolute Stress Fields in the Source Region of the
560 1992 Landers Earthquake. Journal of Geophysical Research-Solid Earth 123, 8874-
561 8890.

562

563 Terakawa, T., Matsu'ura, M., 2008. CMT data inversion using a Bayesian information
564 criterion to estimate seismogenic stress fields. Geophysical Journal International 172,
565 674-685.

566

567 Terakawa, T., Miller, S.A., Deichmann, N., 2012. High fluid pressure and triggered
568 earthquakes in the enhanced geothermal system in Basel, Switzerland. Journal of
569 Geophysical Research-Solid Earth 117.

570

571 Terakawa, T., Zoporowski, A., Galvan, B., Miller, S.A., 2010. High-pressure fluid at
572 hypocentral depths in the L'Aquila region inferred from earthquake focal mechanisms.
573 Geology 38, 995-998.

574

575 Toda, S., Stein, R.S., Lin, J., 2011. Widespread seismicity excitation throughout central
576 Japan following the 2011 M 9.0 Tohoku earthquake and its interpretation by Coulomb
577 stress transfer. Geophysical Research Letters 38, L00G03.

578

579 Wald, D.J., Heaton, T.H., 1994. Spatial and temporal distribution of slip for the 1992
580 Landers, California, earthquake. Bulletin of the Seismological Society of America 84,
581 668-691.

582

583 Yang, W.Z., Hauksson, E., Shearer, P.M., 2012. Computing a Large Refined Catalog of
584 Focal Mechanisms for Southern California (1981-2010): Temporal Stability of the Style
585 of Faulting. Bulletin of the Seismological Society of America 102, 1179-1194.

586

587 Zoback, M.D., Townend, J., 2001. Implications of hydrostatic pore pressures and high
588 crustal strength for the deformation of intraplate lithosphere. Tectonophysics 336, 19-
589 30.

590
591

Table 1 Diagnostic abilities of various stress metrics. ΔE_s, ΔEFS^*, and ΔEFS are evaluated under four background stresses. In each case, the AUC value (green), the true positive rate (red) and false positive rate (blue) at the maximum Youden's index point, and the maximum Youden's index (pink) are shown in a sequential order.

	$C = 0.0$	$C = 0.5$	$C = 0.8$	$C = 1.0$
ΔE_s	0.623	0.641	0.693	0.678
	0.486	0.499	0.572	0.666
	0.124	0.118	0.139	0.378
	0.362	0.381	0.433	0.288
ΔEFS^*	0.682	0.686	0.711	0.706
	0.553	0.582	0.590	0.686
	0.164	0.193	0.191	0.342
	0.389	0.389	0.399	0.344
ΔEFS	0.759	0.760	0.766	0.700
	0.629	0.673	0.654	0.678
	0.159	0.212	0.197	0.342
	0.470	0.461	0.457	0.336
$\Delta \tau_{max}$	0.686 / 0.708 / 0.406 / 0.302			
ΔCFS	0.667 / 0.484 / 0.087 / 0.397			
$ABCS$	0.673 / 0.634 / 0.365 / 0.269			
$SNCS$	0.674 / 0.705 / 0.441 / 0.264			

599 **Figure legends**

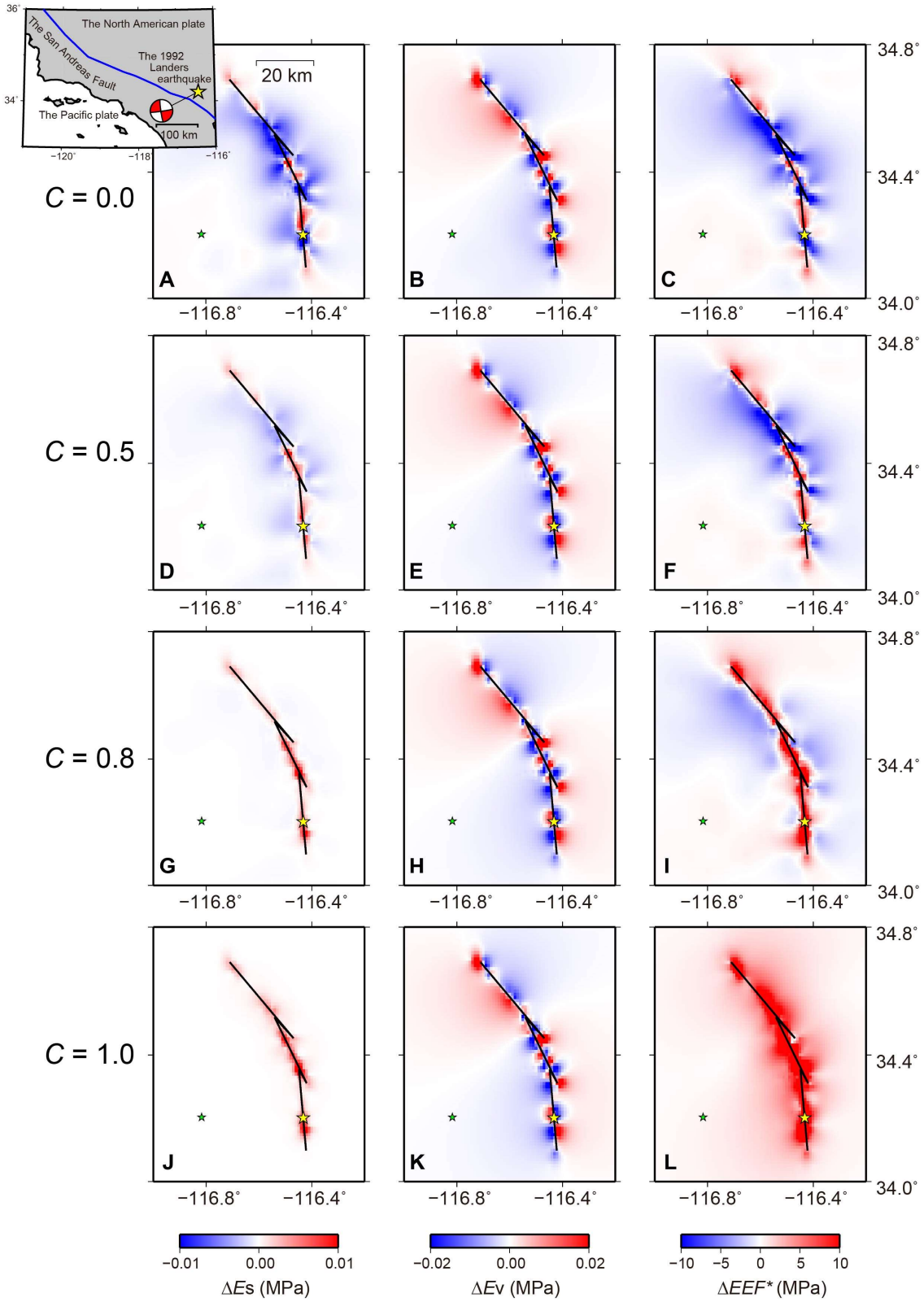

600

Figure 1 Dependence of ΔE_s, ΔE_v, and ΔEFS^* on background stress. The uppermost row (**A**, **B**, and **C**), second row (**D**, **E**, and **F**), third row (**G**, **H**, and **I**), and lowermost row (**J**, **K**, and **L**) show ΔE_s, ΔE_v, and ΔEFS^* at C = 0.0, 0.5, 0.8, and 1.0, respectively. The yellow star and green star indicate the epicenters of the 1992 Landers and 1992 Big Bear earthquakes. The thick black lines denote the fault segments of main rupture of the Landers event. The focal mechanism solution (Yang et al., 2012) for the main shock is shown in the inset.

608

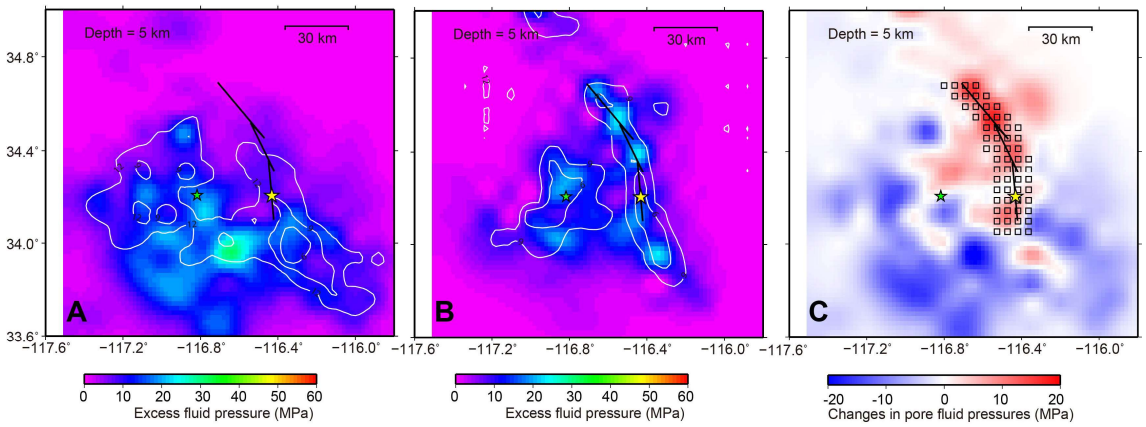

609

610 **Figure 2 Pore-fluid pressure fields in and around the source region of the 1992**
611 **Landers earthquake.** (**A**) Pre-mainshock pore-fluid pressure distribution. (**B**) Post-
612 mainshock pore-fluid pressure distribution. (**C**) Coseismic changes in pore-fluid pressure.
613 We used coseismic pore-fluid pressure changes in the regions with open squares in (**C**) in
614 the analysis of ΔEFS. The yellow star, green star, and thick black lines are the same as
615 those in Figure 1.

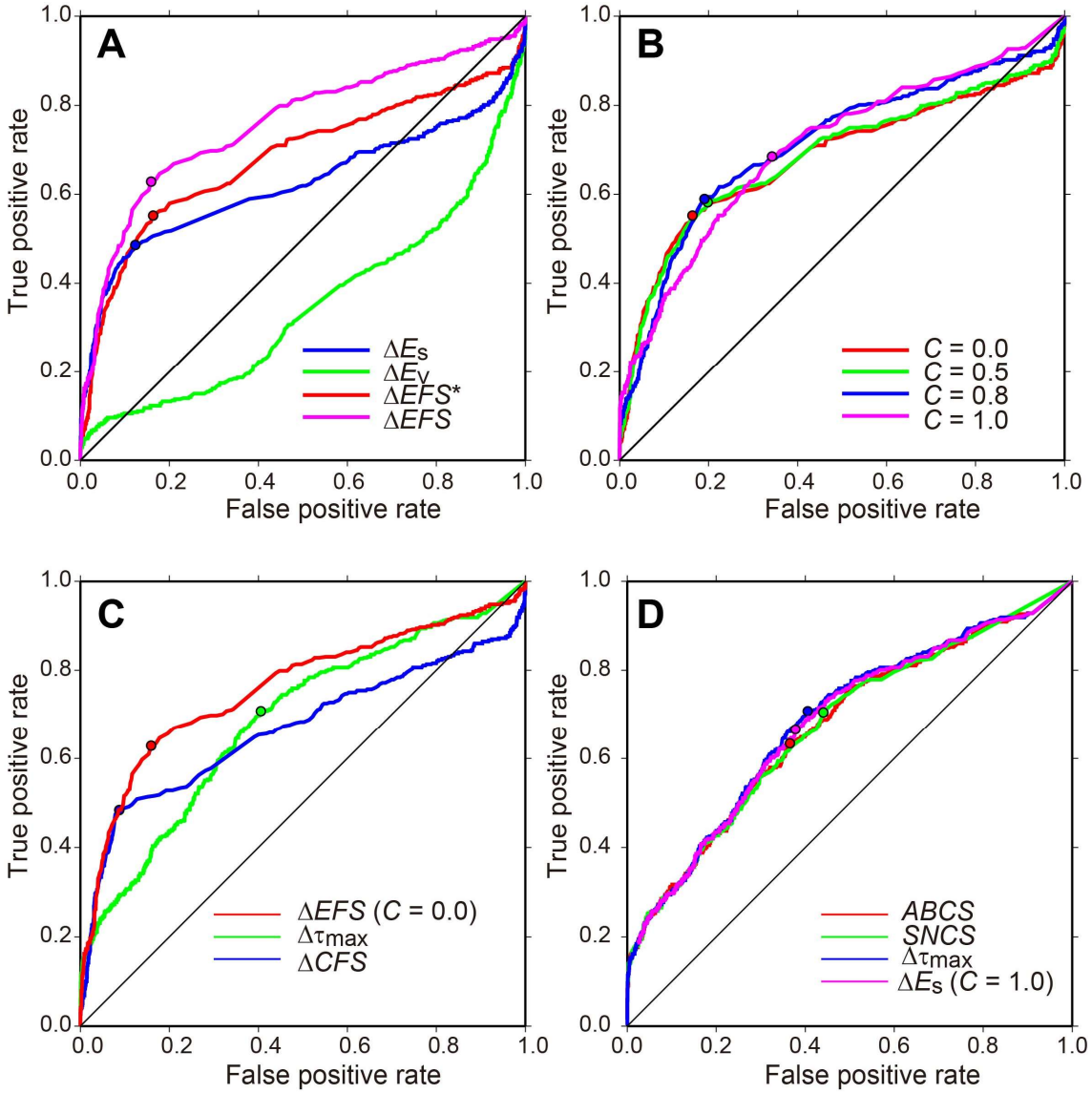

Figure 3 ROC curves for stress metrics. The ROC curves of (**A**) ΔE_s, ΔE_v, ΔEFS^* and ΔEFS for the realistic background stress field (C = 0.0), (**B**) ΔEFS^* for four background stress fields with different deviatoric stress levels, (**C**) ΔEFS (C = 0.0), $\Delta\tau_{max}$, and ΔCFS, and (**D**) *ABCS*, *SNCS*, $\Delta\tau_{max}$, and ΔE_s (C = 1.0). The black lines denote the assessment for random guessing. The coloured circles in (**A**)–(**D**) show true and false

623 positive rates at the maximum Youden's index points. The values of Δ*CFS* in (**c**) were
624 resolved on the plane with similar orientation to the main shock fault.
625

626

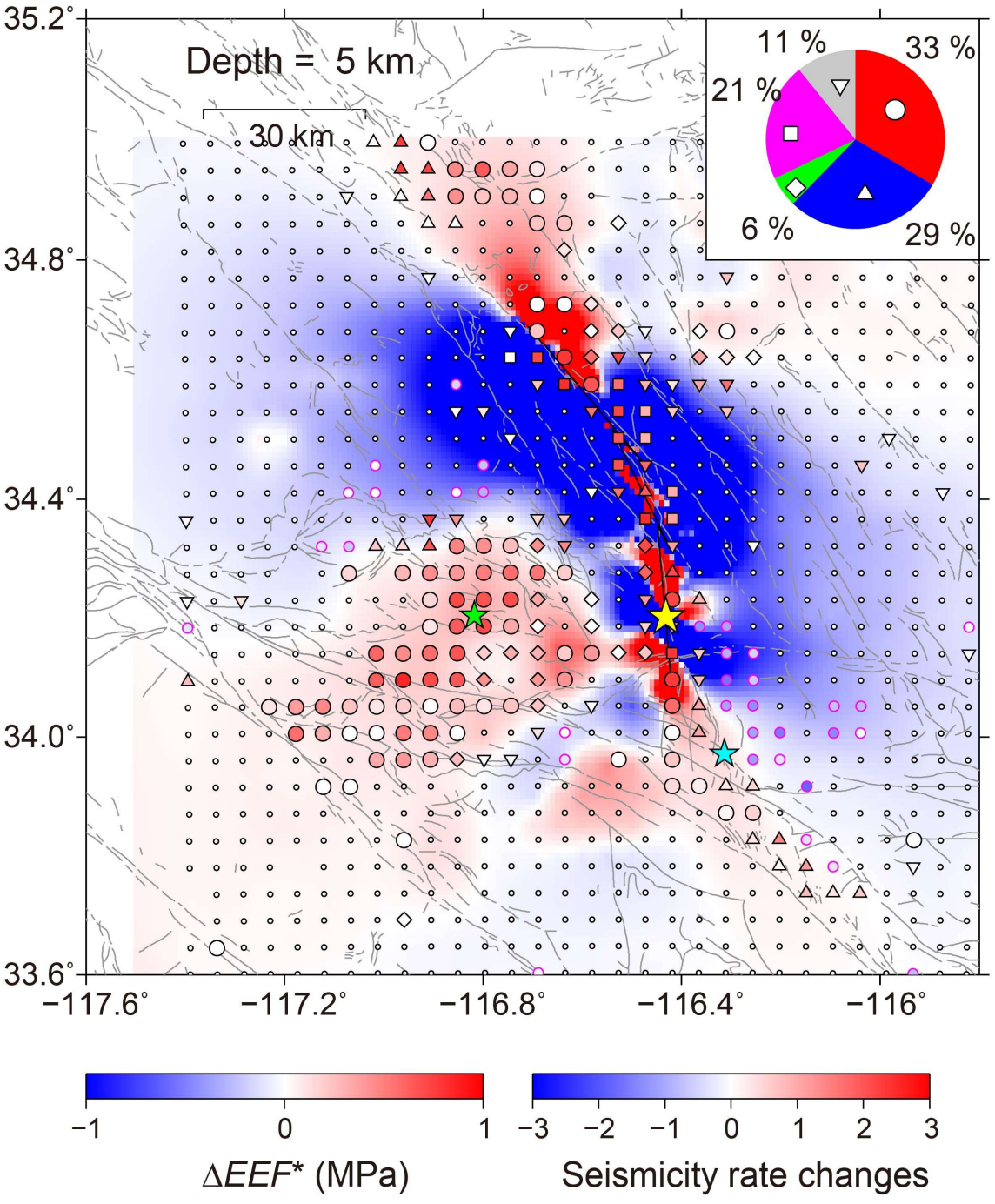

627

628 **Figure 4 Aftershock triggering mechanisms (depth: 2.5–7.5 km).** The shapes of the
629 symbols except the tiny circles, which are plotted in the regions where seismicity has
630 been low throughout the pre- and post-mainshock periods, represent aftershock triggering

631 mechanisms; circle: increase in shear stress (SS) and decrease in fault normal stress (NS),
632 triangle; SS only, squares; NS only, diamond; increase in pore-fluid pressure, inverted
633 triangle; unclear. The pink border circles are plotted in the region where the seismicity
634 rate decreased. The colour scales of these symbols represent the increase (red) or decrease
635 (blue) in seismicity rate (the base 10 logarithm of the number of aftershocks to that of the
636 pre-mainshock period) after the Landers earthquake. The background colour scales
637 indicate the distribution of ΔEFS^* ($C = 0.0$). The pie chart shows the ratios of the whole
638 events across the five classifications. The grey lines denote major Quaternary active faults
639 (Jennings, 1994). The yellow, light green, and light blue starts denote the hypocenters of
640 the 1992 Landers, the 1992 Big Bear, and the 1992 Joshua Tree earthquakes, respectively.

641